HHS Public Access

Author manuscript

J Muscle Res Cell Motil. Author manuscript; available in PMC 2024 December 01.

Published in final edited form as:

J Muscle Res Cell Motil. 2023 December ; 44(4): 271–286. doi:10.1007/s10974-023-09657-1.

THE CRYO-EM 3D IMAGE RECONSTRUCTION OF ISOLATED *LETHOCERUS INDICUS* Z-DISCS

Fatemeh Abbasi Yeganeh[1,6], **Corinne Summerill**[1,2,6], **Zhongjun Hu**[1,3], **Hamidreza Rahmani**[1,4], **Dianne W. Taylor**[1,5], **Kenneth A. Taylor**[1]

[1]Institute of Molecular Biophysics, Florida State University, Tallahassee, FL 32306-4380

[2]Current address: Department of Life and Earth Sciences, Perimeter College, Georgia State University, 33 Gilmer Street SE Atlanta, GA 30303.

[3]Current Address: Facebook, Inc., 1 Hacker Way, Menlo Park, CA 94025

[4]Current Address: The Scripps Research Institute, La Jolla, CA 92037, USA.

[5]Deceased May 17, 2022

[6]These authors contributed equally

Abstract

The Z-disk of striated muscle defines the ends of the sarcomere, which repeats many times within the muscle fiber. Here we report application of cryoelectron tomography and subtomogram averaging to Z-disks isolated from the flight muscles of the large waterbug *Lethocerus indicus*. We use high salt solutions to remove the myosin containing filaments and use gelsolin to remove the actin filaments of the A- and I-bands leaving only the thin filaments within the Z-disk which were then frozen for cryoelectron microscopy. The *Lethocerus* Z-disk structure is similar in many ways to the previously studied Z-disk of the honeybee *Apis mellifera*. At the corners of the unit cell are positioned trimers of paired antiparallel F-actins defining a large solvent channel, whereas at the trigonal positions are positioned F-actin trimers converging slowly towards their (+) ends defining a small solvent channel through the Z-disk. These near parallel F-actins terminate at different Z-heights within the Z-disk. The two types of solvent channel in *Lethocerus* are similar in size compared to those of *Apis* which are very different in size. Two types of α-actinin crosslinks were observed between oppositely oriented actin filaments. In one of these, the α-actinin long axis is almost parallel to the F-actins it crosslinks. In the other, the α-actinins are at a small but distinctive

csummerill@gsu.edu .

Author Contributions:

FAY performed the reconstruction and wrote the paper

CS produced an earlier reconstruction and wrote the paper

DWT isolated the Z-disks and prepared cryoEM specimens

ZH collected the reconstruction data

HR Supervised subtomogram processing

KAT supervised the work and wrote the paper

angle with respect to the crosslinked actin filaments. The utility of isolated Z-disks for structure determination is discussed.

Keywords

α-actinin; kettin; projectin; F-actin; electron tomography

2. Introduction

The Z-Disc is an important structure that defines the ends of the sarcomere in striated muscle, which organizes the thick, myosin-containing and thin, actin-containing filaments and houses many other proteins involved in myofilament stability, signaling, and maintenance of the sarcomere (Frank and Frey, 2011; Frank et al., 2006). The arrangement of thick and thin filaments within the Z-Disc differs between vertebrates and invertebrates. Vertebrates have a rectangular lattice that can assume one of two conformations, small square or basket weave lattices (Knupp et al., 2002), while those Z-disks lattices from invertebrates that are known generally have hexagonal arrangements (Ashhurst, 1967; Cheng and Deatherage, 1989; Saide and Ullrick, 1973; Sainsbury and Hulmes, 1977). The form of the Z-disk is related to the ratio of thin filaments to thick filaments in the A-band. For vertebrates, that ratio is 2:1, while for invertebrates, it is generally 3:1 though reports of ratios as high as 6:1 have occurred (Toselli and Pepe, 1968). The variability in Z-disk lattices from invertebrates is possibly related to the high variability in their thick filament structures. In the past half-century, three-dimensional models and simple diagrams of the Z-Disc have been widely generated from vertebrate muscle samples, such as from mouse psoas myofibrils (Wang et al., 2021), Type 1 Plainfin midshipman fish sonic muscle (Burgoyne et al., 2019), fish fin muscle (Luther, 2000), rat soleus muscle (Yamaguchi et al., 1985) and human patients with nemaline myopathy (Morris et al., 1990). On the other hand, investigations into the structure of Z-Discs of insect flight muscle (IFM) are comparatively sparse, with most of the research done on *Apis mellifera* flight muscle (Cheng and Deatherage, 1989; Deatherage et al., 1989; Rusu et al., 2017; Saide and Ullrick, 1973). The large waterbug *Lethocerus indicus* has served as a model organism for many studies of striated muscle structure and function (Taylor et al., 2019). *Apis* and *Lethocerus* are from two distinct insect orders, Hymenoptera and Hemiptera respectively, both of which utilize asynchronous muscle for flight. A 3-D structure of the *Lethocerus* Z-Disc and with it a comparison with that from *Apis mellifera* could reveal subtle species and order differences as well as evaluating the efficacy of imaging isolated Z-Discs in the unstained, frozen hydrated state.

In the A-band of asynchronous insect flight muscle (IFM), the hexagonal lattice is composed of six thin filaments in the parallel orientation surrounding one thick filament. These thin filaments will progress through the Z-Disc, overlapping with actin filaments from the adjacent sarcomere, and stop just before entering the I-band of the adjacent sarcomere (Fig. 1). The IFM Z-disk structure of *Apis* is unique in that it forms solvent channels of distinctly different sizes and has five types of connecting densities (C1-C5) cross-linking thin filaments of the same or opposite orientation (Deatherage et al., 1989). The large

solvent channel is defined by three pairs of oppositely oriented thin filaments, while the small solvent channel is defined by three actin filaments of the same orientation. In the *Apis* Z-disk, the thin filaments are neither exactly parallel nor antiparallel. Instead the thin filament trimers converge toward the (+) end of the actin filament. Densities, presumably α-actinin, form the C1 and C2 connections between thin filaments of opposite orientation thereby defining the wall of the large solvent channel. In the small solvent channel, densities presumably due to the elastic connecting filaments link thick filaments from one sarcomere with three thin filaments of the adjacent sarcomere. This C4 connection is often depicted as a three-wheel spoke (Cheng and Deatherage, 1989). Thin filaments lining the small solvent channel are linked to six other thin filaments by the C3 and C5 densities. These densities connect the ends of the thin filaments of the small solvent channel to the incoming thin filaments from the adjacent sarcomere.

The composition of the C1, C2, C3, and C5 densities is still relatively unknown, but it is likely that they reveal the locations of Z-Disc proteins. (Cheng and Deatherage, 1989) proposed that C1 and C2 might contain α-actinin, a cross-linking protein that connects thin filaments of opposite orientations, based on their finding that the ~35 nm long protein could fit obliquely in the 17–24 nm space between the actin filaments. Kettin and projectin, two Z-Disc proteins found in IFM, are major components of the elastic connecting filament and are responsible for antiparallel assembly of thin filaments (Kulke et al., 2001; van Straaten et al., 1999) and IFM elasticity (Bullard et al., 2006). Kettin could be crossing between thin filaments of opposite orientation in the Z-Disc (Lakey et al., 1993). Based on more recent studies, projectin is not thought to enter the Z-Disc (Schueder et al., 2023), though may connect with thin filaments outside the Z-Disc (Bullard et al., 2005). This report of a second isolated IFM Z-disk from the hemipteran *Lethocerus indicus* preserved in ice, provides both a comparison with an earlier studies of *Lethocerus* Z-disks (Sainsbury and Hulmes, 1977) and image reconstructions of Z-disks from the hymenopteran *Apis mellifera* in thin plastic sections (Cheng and Deatherage, 1989) and frozen hydrated (Rusu et al., 2017), and provides insight into how these Z-Disc proteins vary between different species and orders of flying insects.

3. Materials and Methods

The generation of a 3D reconstructed *Lethocerus* Z-Disc required samples prepared specifically to show the unique lattice of IFM. The images were processed to extract the hexagonal lattice of thin filaments and the resulting tomograms underwent subtomogram processing to bring out the various structural features in the Z-Disc.

3.1 Sample Preparation

Glycerinated dorsal longitudinal flight muscle of the large waterbug *Lethocerus indicus* was provided by Dr. Michael Reedy of the Department of Cell Biology, Duke University Medical Center. The flight muscle stock was stored in an 80% glycerol-relaxing buffer (10 mM Na_2HPO_4, 100 mM NaCl, 5 mM $MgCl_2$, 5 mM ATP, 5 mM EGTA, pH 7.0) at −80 °C.

Z-Discs were prepared starting with 0.1 ml of muscle myofibrils, which were then washed free of glycerol using glycerol-free relaxing buffer. The myofibrils are centrifuged at 6,000

× g for 2 minutes, turning the tube 3–4 X to form a pellet of myofibrils. The pellet was resuspended in 0.3 ml of high salt buffer (10 mM pyrophosphate, 1.4 M NaCl, 5 mM $MgCl_2$, 5 mM ATP, 5 mM EGTA, pH 8.8) at room temperature to remove myosin filaments. The myofibrils in high salt buffer were checked under a phase contrast microscope for the appearance of stretched myofibrils and brushes coming off the edges of the myofibrils. Exposure to high salt buffer was stopped when too many isolate Z-Discs were observed under the microscope. The sample was centrifuged at 6–7K × g for 2 minutes, turning the tube 3–4X to form a pellet. The pellet was resuspended in a small amount of glycerol-free relaxing buffer (25–30 μl for 0.1 ml of IFM) without homogenization in order to avoid damaging the isolated Z-Discs.

Four μl of sample was placed onto the grid bar side of a reticulated carbon grid for 4–5 minutes. The grid was blotted slightly with filter paper and 3.5 μl of gelsolin (0.3 mg/ml) was added to the grid for about 4.5 minutes for the removal of actin filaments. Gelsolin and remnants of the actin filaments were removed from the grid by rinsing it with rinse buffer (8 mM Na_2HPO_4, 50 mM NaCl, 1 mM $MgCl_2$, 1 mM ATP, 1 mM EGTA, pH 7.0). The grid was either stained with 1% ammonium molybdate or prepared for cryo-EM by manual back blotting (Toyoshima, 1989) and plunge freezing into liquid ethane in a 4°C cold room.

3.2 Data collection

Single axis tilt series with an angle range of ±70° were collected at a temperature of −180 °C at 300 keV on a FEI Titan-Krios electron microscope using a 2° Saxton scheme (Saxton and Baumeister, 1982) and damage compensated motion correction (Wang et al., 2014). A total of 17,627 frames were collected in 191 tilt series. Frames were recorded on a DE-20 direct electron detector (Direct Electron Ltd., San Diego, CA) at 18,000X magnification with a resulting pixel size of 0.203 nm and an overall dose of 90–100 $e^-/Å^2$ per tilt series.

The 0° tilt of the frame aligned images was Fourier transformed to assess the Z-disk spatial order. Tilt series were selected for further processing only if sampled diffraction extended to at least 7.5 nm. Tilt series that included both positive and negative degree tilt angle images were favored in order to increase the efficiency of subtomogram averaging.

3.3. Tilt Series Merging and Contrast Transfer Function Correction

After data collection, the images were processed through an Appion/Leginon/Protomo database-driven pipeline (Noble and Stagg, 2015). The tilt series were initially aligned through the DE Frame Alignment software (Lander et al., 2009). Contrast transfer function correction was then applied to all the images using ACE (Mallick et al., 2005). Next, marker-free coarse alignment of the best tilt series was used to determine if any images in the tilt series needed to be removed because of transfer ice contamination, or faulty tracking (Grant and Grigorieff, 2015; Noble and Stagg, 2015; Winkler and Taylor, 2006; Xiong et al., 2009). Coarse alignment simply aligns an image by a cross correlation against its neighbor image at the lower tilt angle. Coarse alignment was followed by cycles of marker free alignment with area matching (Winkler and Taylor, 2006) in which the reference image is obtained by reprojection of a back projection of previously aligned images.

3.4. Subtomogram Processing

The rest of the image processing was done through the subtomogram processing software I3 (Winkler and Taylor, 2006). A weighted back-projected tomogram was calculated using Protomo, a low-pass filtered map was generated and its Fourier transform computed (Fig. 2a,b). The Fourier transform of the tomogram extended to the (3,3) diffraction spot, indicating that the spatial order out to 8.67 nm resolution. The a* and b* vectors of the diffraction pattern in the Fourier transform were used to compute a spatially averaged 2D or 3D image in the *x*-*y* plane by applying a grid filter in Fourier space to improve the SNR (Supplemental Figure 1).

A reference was made from the spatially averaged map by selecting a region of the image that displayed a clear hexagonal lattice pattern (Supplemental Figure 2a). These positions had the desired motif centered in the input image. The motif in the tomogram is related to “particles” seen in the projection. This motif was then used to compute the cross-correlation map in either 2D projections or 3D volumes (Supplemental Figure 2b). Next a peak search was performed on the projection and positions subsequently refined in 3D from which the real space vectors of the lattice were computed. Coordinates for each motif were generated from the fitted lattice vectors and displayed against the spatially averaged map, and any generated peak coordinates were removed that didn’t fit the lattice pattern or were outside either the image window or the Z-disk boundary (Supplemental Figure 2c). The remaining coordinates containing the center of the subtomograms were placed into a text file and used in I3 for subtomogram alignment.

Before proceeding to the subtomogram alignment step, the subtomograms were rotated about the z-axis to place the “a” axis of the unit cell parallel to the “x” axis of the image raster. This made the subtomogram alignment process proceed faster by reducing the angular alignment. Using the filtered average image, identical locations in adjacent unit cells were picked from which the initial rotation was calculated (Supplemental Figure 3) and used as the first Euler angle.

3.5 Subtomogram Processing: Single- and Multi-Reference Alignment

Subtomograms were roughly centered from the peaks in the cross-correlation map. Nevertheless, their alignment was improved using single reference alignment to the global average to reduce any variation in the initial positions. To make this reference, a cylindrical mask was applied to the global average centered on the large solvent channel at the (0, 0) lattice position but including the six surrounding thin filaments (Supplemental Figure 4). This reference at this point contained few details but possessed the general shape of the object. A polar alignment, which involves the first two Euler angles, was run using this reference to align the individual subtomogram with the Z-axis of the reference followed by a subsequent spin alignment about the reference Z-axis. Multivariate data analysis was then used to produce groups of 2, 4 or 6 class averages for subsequent multireference alignment.

Cycles of multireference alignment over both the polar and spin angles followed by classification produced new references (usually 3–4 new class averages). Alignment cycles were stopped when the details in the subtomograms were satisfactory or showed no

improvement. The related *Apis mellifera* IFM Z-Disc structure was known (Rusu et al., 2017). Once related features were observed in the *Lethocerus* Z-disks, further multi-reference alignment was stopped.

3.6 Symmetry Expansion

We applied symmetry expansion based on the 2-sided plane group symmetry, p321, to obtain additional averaging of the individual thin filaments (Supplemental Figure 5a). Although the Z-disk does not repeat axially, the rotation operations can be applied to the single layered structure. The 2-sided plane group p321 has 3-fold axes perpendicular to the plane of the Z-disk at the corners of the unit cell and 2-fold symmetry axes within the plane of the Z-disk running parallel to the trigonal unit cell axes (Supplemental Figure 5a). Symmetry expansion began by generating a global average with the large solvent channel where the 3-fold and 2-fold axes intersect placed in the middle of the subtomogram (Supplemental Figure 5b). The Fourier transform of this average shows the position of the missing wedge (Supplemental Figure 5c). Then, five additional copies of the global average were generated by applying successively rotations about the 3-fold axis of 120° and 240° followed by a single rotation about the x-axis of 180° (Supplemental Figure 5d). Each rotation generated an additional position file updated for the applied rotations. After applying the rotations, by selecting a single feature in the global average, e.g. a thin filament, the position of the equivalent feature in each subtomogram would be known as was the transformation needed to align that feature within the global average (Supplemental Figure 5e). The Fourier transform of the symmetrized global average shows that the missing wedge has been converted to a missing star-shaped feature (Supplemental Figure 5f). Symmetry expansion resulted in a six-fold increase of the number of thin filament subtomograms that could be averaged to improve the SNR and reduce missing wedge artifacts (Cope et al., 2011) and could be used for subtomogram classification to identify features decorating the thin filaments within the Z-disk.

4. Results

Of the 191 tilt series collected, five were selected for further processing. Many of the tilt series tracked poorly, some only tracked well for the positive angles, some for only the negative angles and some simply failed to merge well for unknown reasons. Of the five selected, three showed particularly good Fourier transforms indicative of a high degree of order. The raw tomograms in general were uninterpretable due to the low contrast within the Z-disk itself (Fig. 2a). Tomograms high in information content could be identified based on the clear hexagonal diffraction pattern in the Fourier transform of the frame-aligned, damage-compensated image at 0° tilt angle and the number of diffraction orders (Fig. 2b). The results shown here were from three of these tilt series with similar angular ranges: Series A, −64° to +48°, Series B, −62° to +48°, and Series C, −64° to +48°. Series A provided a total of 189 subtomograms (before symmetry expansion), Series B provided 187 and Series C provided 121. Symmetry expansion increased the number of thin filament subtomograms by a factor of six.

4.1 Z-disk Filament Lattice

The 3D reconstruction of isolated *Lethocerus* Z-Discs confirms many structural features observed in 3-D image reconstructions of plastic embedded and sectioned *Apis* Z-Disc (Cheng and Deatherage, 1989; Deatherage et al., 1989) as well as frozen-hydrated, isolated *Apis* Z-disks (Rusu et al., 2017). Panning through the raw subtomograms reveals triplets of continuous density that have the morphology of thin filaments (Fig. 3). Each unit cell has a pair of triplets positioned at the trigonal positions polarized in opposite directions, labeled 1 and 2 in the figure. Panning from the middle of the subtomogram in the positive direction, shows that one triplet (Triplet 2) fades away while the other (Triplet 1) continues further, but its density eventually decreases until it also disappears. Triplet 2 terminates at its (+) end. The position of the quasi-3-fold axis of Triplets 1 and 2 represents the location of a thick filament further down in the A-band. Triplet 2 disappears because the thin filament continuation at the actin (−) end has been truncated irregularly by the gelsolin treatment. Conceivably, Triplet 1 does the same on the other side of the Z-disk. Both triplets follow converging trajectories towards their (+) end but in opposite directions due to their opposing orientation within the Z-disk unit cell (Deatherage et al., 1989). Once thin filaments enter the Z-disk they follow a slightly converging trajectory towards their (+) end.

These same features are observed in surface views of the symmetrized global averages (Fig. 4). Although we used symmetry expansion to increase the subtomogram numbers, the symmetry was not quantitatively imposed on the averages, so they show some asymmetry. Each unit cell contained six thin filaments, three filaments each with opposite orientations (Fig. 4a). To produce the arrangement of six thin filaments surrounding each thick filament in the A-band dictates that each of the three trimers (magenta) surrounding a thick filament location (green disk) contribute two filaments each. The three thin filaments in the center (green) surrounding the green disk terminate at the edge of the Z-disk and do not extend into the A-band with the thin filaments of the magenta trimers.

When observing the Z-Disc from the side, filaments do not progress in parallel through the entire isolated Z-Disc (Fig. 4b) but instead converge toward their (+) ends which point toward the thick filament positions in the adjacent A-band. Filaments of opposite orientation overlap for a distance of ~90 nm, which is a value close to the ~80 nm overlap found in *Apis* Z-Discs (Cheng and Deatherage, 1989). The difference could easily be due to mass loss in the *Apis* thin plastic sections caused by excessive electron exposure (Thach and Thach, 1971).

Decreasing the density threshold of the symmetrized global average revealed a network of connecting densities that maintains the arrangement of the thin filaments of opposite and similar orientations (Fig. 5a,b). The thin filament connections define the two different channels: the large channel formed by six thin filaments of alternating polarity at the apices of each unit cell, and the two small solvent channels within the unit cell formed by three thin filaments of the same polarity at the trigonal positions (Fig. 5b). The distance between the centers of adjacent small solvent channels of the same polarity was ~52 nm, which is nearly equivalent to the inter-thick-filament spacing found in *Lethocerus* IFM (Tregear et al., 1998) indicating that the Z-disk lattice matches in spacing the A-band lattice.

4.2 The Solvent Channels

A distinct difference between the *Lethocerus* and *Apis* Z-disks is illustrated in the Fourier transforms of the image recorded at 0° tilt as well as the central section of the Fourier transform of the tomogram. In *Apis*, the 1,0 spot is strong (Rusu et al., 2017), but in *Lethocerus*, the 1,0 spot is weak or absent (Fig. 2b). Another difference is in the 2,0 spots, which are weak in *Apis* (Cheng and Deatherage, 1989; Rusu et al., 2017), but strong in *Lethocerus*. In *Apis*, two distinctly different sizes of solvent channel have been described (Saide and Ullrick, 1973). The large solvent channel is positioned at the corners of the unit cell, where six actin-filament trimers of alternating polarity contribute one thin filament each. The small solvent channel is within the actin filament trimers themselves positioned at the trigonal positions of the unit cell (Fig. 5). The large solvent channel in *Apis* is considerably larger than the small channel because of the strong convergence angle of the *Apis* thin filaments. However, in *Lethocerus*, the large and small solvent channels are of approximately equal size (Fig. 6) resulting in a weak 1,0 spot and a strong 2,0 spot. Thus, the 1,0 spot in the Fourier transform of the isolated Z-disks from asynchronous flight muscle can be diagnostic of the size difference between large and small solvent channels. This observation may also hold for other trigonal Z-disks in invertebrate striated muscles from different sources.

Saide and Ullrick (1973) first identified the triangular solvent channels in the *Apis* Z-Disc and noted that the large solvent channel rotated by 60° from one side of the Z-Disc to the other. The shape of the small solvent channel undergoes no rotation when traversing the Z-disk from one side to the other. The equivalent large solvent channel in *Lethocerus* is not as obvious because of its smaller size, but can be identified by its location at the vertices of the unit cell. At section 0, the middle of the Z-Disc, there appears to be a hexagonal structure formed by the interaction of six thin filaments of alternating polarity held together via connecting densities (Figs. 3,6). Polarity in this case being defined by whether the thin filament was contributed by Trimer 1 (sarcomere A) or 2 (sarcomere B) in the adjacent unit cells. From section ±20 and onward, the small solvent channels keep the same orientation but their size, illustrated by the size of the triangle, changes only slightly from one side of the Z-disk to the other consistent with the small convergence angle toward the (+) end.

Saide and Ullrick (1973) were able to follow the large and small solvent channels for greater distance because they were examining thin plastic sections and concluded that the shape of the large solvent channel rotated 60° from one side of the Z-disk to the other. The present result, which is based on isolated Z-disks does not continue far enough into the I-bands to show this rotation convincingly. Differences in our sample preparation, isolated Z-Discs vs plastic sections of muscle fibers, prevent us from tracking the thin filaments all the way to the A-band. Nevertheless, the isolated Z-disks are consistent with the earlier results while being differentiated principally by the relative size of the solvent channels and consequently the convergence angle of the thin filaments.

4.3 Connecting Densities

Like the *Apis* Z-disk, the *Lethocerus* Z-disk has numerous densities connecting both parallel and antiparallel thin filaments. (Cheng and Deatherage, 1989) reported five connecting

densities, C1-C5, in their reconstruction, two of these, C1 and C2, were hypothesized to contain the F-actin cross-linking protein α-actinin. Other densities appear to connect thin filaments, sometimes of the same and sometimes of the opposite polarity. In the middle of the tomogram, six densities (thin filaments) appear to form groups enclosed by connections.

When the contour threshold is lowered, connecting densities between thin filaments appear which we identify with the previously described C1, C2, C3 and C5 connections (Cheng and Deatherage, 1989). The connection C1 we identify with the outward-bowing density that connects antiparallel thin filaments centered at the corners of the unit cell (colored green in Figure 3). The connection C2 we identify with the inward bowing density (colored blue in Figure 3). The C1 connection, the length of which depends on the contour threshold, is particularly well defined and extends for >80 nm along the Z-axis (Fig. 4). The C2 connector is less well defined. We suspect that both C1 and C2 in the average image comprise crosslinks with some degree of variation along the Z-axis of the structure.

In the density map of the large solvent channel, we were able to insert a density map computed from a human muscle α-actinin atomic model (PDB ID: 4D1E; (Ribeiro Ede et al., 2014)), length of ~40 nm, into the C1 connecting density, of ~55 nm in length (Fig. 7c,d). The α-actinin model was aligned parallel to the adjacent thin filaments.

The C2 connection was less easy to identify because it appears more disordered. In the global average, C2 appears as separate small connections indicative of a high degree of variation. To separate some of the variants, we used multivariate data analysis. An annular mask that excluded the actin filament while including space for any surrounding features was used for the classification. After 15 cycles of multireference alignment using just the segmented aligned actin filaments, we could identify an extended density of a length appropriate to α-actinin. This presumed α-actinin crosslink is at an oblique angle to the actin filament, unlike the C1 density (Fig. 7c,d), which is largely parallel. By mapping back into the symmetrized global average, we identified an extended crosslink at the C2 position (Fig. 3). The α-actinin model that was used for the C1 density also fit into the density at an oblique angle with the ends connecting relatively well with the F-actin models.

We think that the fact that the C2 connecting density is at an oblique angle to the filament axis, whereas the C1 connector is parallel to the filament axis is the reason for the weak C2 density. If C1 connectors are positioned at the different Z-heights, for reasons that will be explained below, they will still superimpose at least over some of their length to contribute a strong density in the average. On the other hand, the C2 connectors, which are angled will not superimpose well unless they are located at the same Z-position.

Near the edge of the *Lethocerus* Z-Disc, a pair of densities, C3 and C5, connect the end of one thin filament to a thin filament of opposite orientation (Fig. 7a,b). C5 type connections were found at the bases of the triangle in the large solvent channel, while C3 type connections were located at the apices of that triangle.

4.4 Actin Filaments

To observe more details of the actin filaments, such as the actin subunits or other actin-binding proteins such as kettin, we extracted all the individual actin filaments from the raw tomogram, using the position file of the global average to obtain their locations in the raw Z-disk tomograms. These were then aligned first to a featureless cylinder of appropriate diameter in order to align their filament axes. Twenty cycles of multireference alignment using thin filament class averages were then performed. The long pitch helical track of the actin filament was clearly visible (Fig. 8a,b). The resulting class averages did not resolve individual actin subunits or even locations where connecting densities might occur, but they did show the long-pitch helical track representative of actin filaments (Fig. 8a,b). An F-actin atomic model was used to compute a density map for placement into the final density of class averages (Fig. 8c). Based on Relion_helix_toolbox the helical rise of the F-actin global average was 2.879 nm and the helical twist is −167.408° which is very close to the genetic helix twist of F-actin, 167.14°, for the 28/13 F-actin helix typical of *Lethocerus* flight muscle (Holmes et al., 1980).

The missing cone in our data could be affecting our ability to see fine details on the actin filaments. The orientation of the actin filaments in isolated Z-disks is highly unfavorable for resolving actin subunits because most of the 5.9 nm and 5.1 nm layerline amplitude falls inside of the missing wedge. However, the averaged F-actin density and the inverse of the alignment matrix permitted placement of the F-actin model density into our Z-Disc density maps based solely on the long-pitch helix (Fig. 8c) which gives an uncertainty in the axial position of an actin subunit of ±2.75 nm.

4.5 The A-Bee-Z Problem

The symmetry in the Z-disk of asynchronous flight muscle is somewhat controversial. In the original publication the symmetry of the *Apis* Z-disk was said to be p312 (Deatherage et al., 1989), using the nomenclature for 2-sided plane groups (Amos et al., 1982). This was possibly a misprint. The difference between p312 and p321 lies in the position of the 2-fold axes in the center of the Z-disk plane, which lie perpendicular to the unit cell edges in p312 and parallel to the unit cell edges in p321. The density maps shown in the original publication are consistent with p321.

Squire (1992) pointed out that the Cheng and Deatherage 3D of the *Apis* Z-disk reconstruction, which utilized only rotational symmetry operations and no screw axis operations, when extrapolated into the A-band, implies rings of target zones rather than helices of target zones surrounding the thick filament. Target zones are defined as the regions of the thin filament where the azimuth is favorable to strongly bound myosin heads (Holmes et al., 1980; Reedy, 1968; Wu et al., 2010). The A-band lattice of *Lethocerus* flight muscle has six thin filaments surrounding each myosin filament. Each thin filament is placed midway between pairs of myosin filaments. The target zones of the *Lethocerus* thin filaments are located midway between successive troponin complexes and follow a left-handed $P6_4$ helix (Holmes et al., 1980), in which thin filaments rotate 60° in a left-handed (clockwise) sense about the thick filament axis and translate 12.9 nm axially. The troponin complex moves with the thin filament and is the origin of the strong 12.9 nm meridional in

Lethocerus flight muscle X-ray fiber diagrams. After six such movements, the thin filament has translated axially by 77.4 nm, one full pitch. Space group $P6_4$ is only possible if the thin filaments have a random 180° azimuthal rotation, which appears to be the case (Holmes et al., 1980).

The discrepancy might be resolved if positions on each of the actin filaments at the trigonal positions are related by 3-fold screw axes perpendicular to the plane in the insect Z-band instead of 3-fold rotation axes. Strictly speaking such axes cannot occur because the (+) ends of the thin filament trimers converge toward their 3-fold axis but must run parallel to each other if the screw symmetry is to be strictly obeyed. Nevertheless, the actin filaments within the Z-disk may still show features of a 3-fold screw axis even if it is not precise.

The six thin filaments that surround each thick filament in the A-band are provided by two of the thin filaments from each of the three Z-disk trimers that surround the thick filament position in the Z-disk (Fig. 9a,b, gray disk). The target zone symmetry, in the notation of the International Tables for X-ray Crystallography, requires that a point in the lattice, "+", be translated axially by $1/3^{rd}$ of the axial repeat, 12.9 nm, and rotated clockwise by 60° (Fig. 9a). The process is repeated for each of the six thin filaments surrounding a thick filament. Because of the random azimuthal disorder in the thin filaments, the structure repeats after only three operations (38.67 nm) rather than the true pitch of the thin filament which is twice that value. The process is repeated around each thick filament, each of which shares a thin filament with another thick filament. If the process is repeated laterally, a set of rotations and axial translations for each thin filament is generated. If the thin filaments in the Z-disk were parallel instead of converging at their (+) ends, the *Lethocerus* Z-disk would be described by space group $P3_121$ (right-handed) instead of the 2-sided plane group p321 assumed by Cheng and Deatherage. When the process is repeated for each polarized set of thin filaments a regular lattice is generated (Fig. 9a,b). When the two polarized lattices are put together to form the Z-disk, the 2-fold axes that would be positioned within the center of the Z-disk in p321 are no longer confined to the middle of the Z-disk but instead are replaced by rotation axes at three different z-levels, though still running parallel to the unit cell axes. Thus, single crosslinks between antiparallel thin filaments by α-actinin would occur at three different levels along the z-axis.

We searched for some evidence of screw symmetry relating the thin filaments of some trimers using the global average generated previously (Fig. 8c). We generated a thin filament density map with a fiducial of one missing actin subunit and a second thin filament map with just the fiducial actin subunit, which could be colored differently. Using the inverse of the individual thin filament alignment matrices used to generate the global actin average, we "mapped back" this fiducial-marked thin filament into all the thin filament positions within the Z-disk. The operation did not reveal the predicted screw axes (Fig. 9e,f,g), The exercise did show that the thin filaments within the trimer were not related by a simple rotation axis but the amount of displacement was of about the same as the axial uncertainty of actin subunits within the global average.

The C1 connecting densities, which most likely, but not certainly, arise from α-actinin crosslinks are too long (80 nm) to be single α-actinin crosslink, but might be averages of

three different α-actinin crosslinks offset axially by 12.9 nm. Because C1 crosslinks run parallel to the thin filaments, they will superimpose partially even if axially disordered. For example, α-actinin is ~36 nm long (Ribeiro Ede et al., 2014) while the offsets required by the screw symmetry are 12.9 nm long or about 1/3rd the length of α-actinin. The extended length and clarity of the C1 crosslinks would be explained by the persistent 2/3^{rds} overlap of α-actinins. The C2 crosslinks, which are angled, would not superimpose well if offset axially by 12.9 nm and thus can only be detected by subtomogram classification. Nevertheless, the connecting densities do not provide convincing evidence for the presence of screw axes within the Z-disk. The question may require reconstructing the Z-disk from focused ion beam milling of myofibrils, where the orientation of the thin filaments and crosslinks are more favorable.

5. Discussion

5.1. Comparison with Previous Work

Our 3D reconstruction of the isolated, frozen-hydrated *Lethocerus* Z-Disc is largely consistent with previous results from 3-D imaging of *Apis mellifera* flight muscle Z-Discs (Cheng and Deatherage, 1989; Rusu et al., 2017). Features that are in common to both 3D images are the hexagonal lattice arrangement of thin filaments, the presence of large and small solvent channels, and connecting densities C1-C5. However, more questions still need to be answered about these features.

The identity of the C3 and C5 connecting densities are still unknown due to lack of structural information in our data, but it could be possible that these densities represent the crossing of kettin between thin filaments of opposite orientation as proposed by (Lakey et al., 1993). C3 and C5 appear near the edge of the Z-Disc and seem to branch down into the Z-Disc from the incoming thin filaments as they interact with the thin filaments of opposite orientation. As the N-terminus of kettin was found to be located in the middle of the Z-Disc (van Straaten et al., 1999) and ~54 nm of *Lethocerus* kettin is located inside the Z-Disc, its considerable length makes it possible for it to cross between antiparallel thin filaments and might even interact with α-actinin in the C1/C2 densities. As one of the functions of kettin is the antiparallel assembly of thin filaments, this protein needs to connect filaments of opposite orientations to complete its function.

The binding site of kettin Ig domains on F-actin was recently determined using the homologous Filamin Ig domains (Suphamungmee et al., 2012). To the extent that IFM kettin Ig domains are similar to those of filamin, the result suggest they specifically lie along the actin-helix over the N-terminus of actin subdomain 1 and would be consistent with the hypothesis that kettin runs along the genetic helix of F-actin positioned on actin subdomain 1 and overlapping actin subdomain 3 (Bullard et al., 1999). With this information and if our data had a sufficient signal-to-noise ratio that brought out the details of the individual actin subunits, we could reconstruct a model showing the path of kettin in the Z-Disc. Lastly, a question that would need be answered about kettin is does it interact with CapZ, an actin-capping protein that binds to the barbed end of the actin? C5 does appear to interact with the top of the actin filament (Fig. 7b), so either there is a direct connection between the two proteins or kettin narrowly misses CapZ.

Based on our results, we propose that C1 and C2 are connecting densities containing α-actinin. In C1, α-actinin appears to be oriented parallel to the axis of the thin filaments, while α-actinin in C2 orients at an oblique angle relative to the thin filament axis. Our model of C2 in relation to CH1 domain on F-actin showed that the atomic model of α-actinin was able to fit in the space between the two thin filaments and almost touch the CH1 bound to F-actin. The ability for this cross-linker protein to connect actin filaments in a variety of orientations (Hampton et al., 2007) relies on flexible linkers between the actin binding domain and the rest of the molecule.

Within the “head” domain of α-actinin, a linker connects the CH1 and CH2 domains. It was found that this linker gives the ability for the ABDs to rotate 90° relative to each other (Liu et al., 2004). Besides rotation within the “head” domain, a 25–30 residue flexible linker, specified as the “neck” region, connects CH2 to the “rod” domain to allow rotation of the entire “head” domain (Imamura et al., 1988). Lastly, the CaM-like domain can rotate 180° about its linker to R4 (Liu et al., 2004). With these additional details, an α-actinin atomic model in a variety of rotational orientations might be possible with a higher resolution density map.

The cryo-EM 3D reconstruction of isolated *Apis* Z-Discs (Rusu et al., 2017) was limited by excessive radiation damage during collection of the tilt series. Some structural features seen in this study, for example an α-actinin like density was observed but could not be assigned to C1 or C2 and the C3-C5 connections were ambiguous. However, the *Apis* tomograms clearly showed the large solvent channel rotation which was not as obvious in *Lethocerus*. In the future, the presence of large and small channels in the Z-disk may be predictable by differences in the intensity of (1,0) and (2,0) spots in the diffraction patterns of the Z-Disc samples.

5.1. Thin Filament Symmetry within Isolated Z-Discs

In the flight muscles of *Lethocerus*, the symmetry of target zones within the A-band is well established (Holmes et al., 1980). Target zones and troponin complexes follow a left-handed helical path around each thick filament with each successive thin filament rising 12.9 nm and rotating 60° in a left-handed sense. The target zone symmetry within *Apis* flight muscle is less well established but most likely very similar. The possibility that the thin filament arrangement differs from that of *Lethocerus* is not small. In *Drosophila*, for example, the thick filaments are arranged in a superlattice (Squire et al., 2006), which may alter the arrangement of thin filaments in the A-band and consequently in the Z-disk. The arrangement of thin filaments in the *Apis* Z-disk was suggested to conform to the two-sided plane group, p321, which is inconsistent with the well-established arrangement of thin filaments in the A-band of *Lethocerus* (Squire, 1992).

5.2 Utility of Isolated Z-Discs

This work is only the second attempt to image a Z-Disc isolated from striated muscle. The potential benefit of our approach is that it removes the necessity of dehydration, embedding, sectioning and staining of muscle tissue for ultramicrotomy. The helical structure of actin is difficult to preserve under conditions of conventional fixation (Lehrer, 1981; Maupin-

Szamier and Pollard, 1978) and only in certain instances, importantly one of these is for insect flight muscle, has the F-actin helical structure been demonstrated in plastic sections (Reedy et al., 1987; Reedy et al., 1983). Use of negative stains such as uranyl acetate and uranyl formate (Hanson and Lowy, 1963; Huxley, 1963) as well as ice embedded specimens (Milligan and Flicker, 1987) have been the only preparation methods that so far have maintained F-actin's helical structure for electron microscopy. Isolation of Z-disks had been reported as far back as 1974 (Saide and Ullrick, 1974) and might have been pursued as an alternative that better preserves the structure of F-actin using uranyl acetate stains.

Ice-embedded specimens are generally considered the optimal preservation medium for biological structure (Carroni and Saibil, 2016). However, with a tissue such as muscle, such specimens need to be either cryosectioned and viewed as frozen sections or thinned by Focused Ion Beam (FIB) milling to a thickness small enough for cryoET. Cryosections suffer from section compression (Al-Amoudi et al., 2005), while FIB milling is a slow and tedious technique (Dubrovsky et al., 2015).

When imaged by EM, stained, plastic longitudinal sections of *Lethocerus* flight muscle fibers show highly electron dense Z-Discs with little regularity (Reedy, 1967). The structure appears full of accessory proteins rather than the purely structural proteins that are expected. Some of this "extra" protein may come from the flight muscle thick filament proteins flightin and myofilin, which migrate from a soluble pool to the Z-Disc when the muscle is stored in glycerol for a prolonged period (Ferguson et al., 1994). Our raw tomograms of isolated *Lethocerus* Z-Discs could be contaminated in this way because the tissue had been glycerinated for a considerable time. The only previous study of *Lethocerus* Z-disk structure using plastic sections from freshly dissected muscle showed a similar electron dense electron micrograph with a much clearer averaged image (Sainsbury and Hulmes, 1977). Filtered images of these sections are quite detailed.

Our reconstruction, coming as it did from a limited number of tomograms and a small number of subtomograms is surprisingly detailed. Topologically, isolated Z-Discs with their plane oriented perpendicular to the optical axis and F-actin oriented approximately parallel to the optical axis are in the worst possible orientation for 3-D imaging of actin subunits. If the procedures initiated in this study can resolve the F-actin subunits, then the resolution is high enough to identify other proteins within the Z- disk that stabilize it or are involved in signal transduction. The difficulty of the problem can be visualized using the X-ray diagram from rigor *Lethocerus* flight muscle (e.g. Fig. 2 of (Holmes et al., 1980)).

When the actin filaments are oriented parallel to the optical axis, how much of their Fourier transform that can be measured depends highly on the maximum tilt angle. Typically, the highest accessible tilt angle is 70° which leaves the inner most regions inaccessible. Although we recorded images to angles as high as 70°, we often could not use the highest tilt angles and thus the portion of the layer lines from the actin genetic helices is even smaller. The problem is ameliorated somewhat by the fact that within the Z-Disc itself, the actin filaments are oriented at an angle of 80–84° relative to the plane of the Z-Discs, which effectively tilts the filaments to a higher angle thereby accessing more of the transform of the 13^{th} and 15^{th} layer lines. Thus, the crucial problem to be resolved in the future is how

to utilize the highest tilt angles. Nevertheless, that this study came close to resolving actin subunits suggesting that the problem is tractable.

Supplementary Material

Refer to Web version on PubMed Central for supplementary material.

Acknowledgements

This research was supported by NIH grants R01 GM30598 and R35 GM139616 to KAT. The Titan was partially funded from NIH grant S10 RR025080 with funds for the DE-20 provided by S10 OD018142. ZH and HR were funded by American Heart Association predoctoral fellowships 15PRE25090150 and 20PRE35120273 respectively. We thank Dr. Belinda Bullard for her comments on an earlier version of the manuscript and Dr. Alimohammed Hojjatian for his assistance in the data upload. We dedicate this paper to the late Prof. John Trinick who stimulated our interest in studying the invertebrate Z-disk structure.

Data Availability

The tomograms and subtomogram averages have been deposited into the EMDB under accession code EMDB-41124 and the raw data deposited in EMPIAR under accession code EMPIAR-11594.

Bibliography

Al-Amoudi A, Studer D, Dubochet J, 2005. Cutting artefacts and cutting process in vitreous sections for cryo-electron microscopy. J Struct Biol 150, 109–121. doi: 10.1016/j.jsb.2005.01.003. [PubMed: 15797735]

Amos LA, Henderson R, Unwin PN, 1982. Three-dimensional structure determination by electron microscopy of two-dimensional crystals. Prog Biophys Mol Biol 39, 183–231. doi: 10.1016/0079-6107(83)90017-2. [PubMed: 6289376]

Ashhurst DE, 1967. Z-line of the flight muscle of belostomatid water bugs. J Mol Biol 27, 385–389. doi: 10.1016/0022-2836(67)90027-7. [PubMed: 6048987]

Bullard B, Goulding D, Ferguson C, Leonard K, 1999. Links in the chain: the contribution of kettin to the elasticity of insect muscles, p. 207–220, in: Pollack G and Granzier H, Eds.), Elastic Filaments of the Cell. Kluwer Academic Press, Boston, MA.

Bullard B, Burkart C, Labeit S, Leonard K, 2005. The function of elastic proteins in the oscillatory contraction of insect flight muscle. J Muscle Res Cell Motil 26, 479–485. doi: 10.1007/s10974-005-9032-7. [PubMed: 16450058]

Bullard B, Garcia T, Benes V, Leake MC, Linke WA, Oberhauser AF, 2006. The molecular elasticity of the insect flight muscle proteins projectin and kettin. Proc Natl Acad Sci U S A 103, 4451–4456. doi: 10.1073/pnas.0509016103. [PubMed: 16537423]

Burgoyne T, Heumann JM, Morris EP, Knupp C, Liu J, Reedy MK, Taylor KA, Wang K, Luther PK, 2019. Three-dimensional structure of the basketweave Z-band in midshipman fish sonic muscle. Proc Natl Acad Sci U S A 116, 15534–15539. doi: 10.1073/pnas.1902235116. [PubMed: 31320587]

Carroni M, Saibil HR, 2016. Cryo electron microscopy to determine the structure of macromolecular complexes. Methods 95, 78–85. doi: 10.1016/j.ymeth.2015.11.023. [PubMed: 26638773]

Cheng NQ, Deatherage JF, 1989. Three-dimensional reconstruction of the Z disk of sectioned bee flight muscle. J. Cell Biol 108, 1761–1774. doi: 10.1083/jcb.108.5.1761. [PubMed: 2715176]

Cope J, Heumann J, Hoenger A, 2011. Cryo-electron tomography for structural characterization of macromolecular complexes. Curr Protoc Protein Sci Chapter 17, Unit17 13. doi: 10.1002/0471140864.ps1713s65.

Deatherage JF, Cheng NQ, Bullard B, 1989. Arrangement of filaments and cross-links in the bee flight muscle Z disk by image analysis of oblique sections. J. Cell Biol 108, 1775–1782. doi: 10.1083/jcb.108.5.1775. [PubMed: 2715177]

Dubrovsky A, Sorrentino S, Harapin J, Sapra KT, Medalia O, 2015. Developments in cryo-electron tomography for in situ structural analysis. Arch Biochem Biophys 581, 78–85. doi: 10.1016/j.abb.2015.04.006. [PubMed: 25921875]

Ferguson C, Lakey A, Hutchings A, Butcher GW, Leonard KR, Bullard B, 1994. Cytoskeletal proteins of insect muscle: location of zeelins in Lethocerus flight and leg muscle. J Cell Sci 107 (Pt 5), 1115–1129. [PubMed: 7929622]

Frank D, Frey N, 2011. Cardiac Z-disc signaling network. J Biol Chem 286, 9897–9904. doi: 10.1074/jbc.R110.174268. [PubMed: 21257757]

Frank D, Kuhn C, Katus HA, Frey N, 2006. The sarcomeric Z-disc: a nodal point in signalling and disease. J Mol Med (Berl) 84, 446–468. doi: 10.1007/s00109-005-0033-1. [PubMed: 16416311]

Grant T, Grigorieff N, 2015. Measuring the optimal exposure for single particle cryo-EM using a 2.6 A reconstruction of rotavirus VP6. Elife 4, e06980. doi: 10.7554/eLife.06980. [PubMed: 26023829]

Hampton CM, Taylor DW, Taylor KA, 2007. Novel structures for alpha-actinin:F-actin interactions and their implications for actin-membrane attachment and tension sensing in the cytoskeleton. J Mol Biol 368, 92–104. doi: 10.1016/j.jmb.2007.01.071. [PubMed: 17331538]

Hanson J, Lowy J, 1963. The structure of F-actin and of actin filaments isolated from muscle. J Mol Biol 6, 46–60. doi: 10.1016/s0022-2836(63)80081-9.

Holmes KC, Tregear RT, Barrington Leigh J, 1980. Interpretation of the low angle X-ray diffraction from insect muscle in rigor. Proc. Roy. Soc. (London) - Series B: Biological 207, 13–33.

Huxley HE, 1963. Electron microscope studies on the structure of natural and synthetic protein filaments from striated muscle. J Mol Biol 7, 281–308. doi: 10.1016/s0022-2836(63)80008-x [PubMed: 14064165]

Imamura M, Endo T, Kuroda M, Tanaka T, Masaki T, 1988. Substructure and higher structure of chicken smooth muscle alpha-actinin molecule. J Biol Chem 263, 7800–7805. [PubMed: 3286641]

Knupp C, Luther PK, Squire JM, 2002. Titin organisation and the 3D architecture of the vertebrate-striated muscle I-band. J Mol Biol 322, 731–739. doi: 10.1016/s0022-2836(02)00819-7. [PubMed: 12270710]

Kulke M, Neagoe C, Kolmerer B, Minajeva A, Hinssen H, Bullard B, Linke WA, 2001. Kettin, a major source of myofibrillar stiffness in Drosophila indirect flight muscle. J. Cell Biol 154, 1045–1057. doi: 10.1083/jcb.200104016. [PubMed: 11535621]

Lakey A, Labeit S, Gautel M, Ferguson C, Barlow DP, Leonard K, Bullard B, 1993. Kettin, a large modular protein in the Z-disc of insect muscles. EMBO J 12, 2863–2871. doi: 10.1002/j.1460-2075.1993.tb05948.x. [PubMed: 8335002]

Lander GC, Stagg SM, Voss NR, Cheng A, Fellmann D, Pulokas J, Yoshioka C, Irving C, Mulder A, Lau PW, Lyumkis D, Potter CS, Carragher B, 2009. Appion: an integrated, database-driven pipeline to facilitate EM image processing. J Struct Biol 166, 95–102. doi: 10.1016/j.jsb.2009.01.002. [PubMed: 19263523]

Lehrer SS, 1981. Damage to actin filaments by glutaraldehyde: protection by tropomyosin. J. Cell Biol 90, 459–466. [PubMed: 6793598]

Liu J, Taylor DW, Taylor KA, 2004. A 3-D reconstruction of smooth muscle alpha-actinin by cryoEM reveals two different conformations at the actin-binding region. J Mol Biol 338, 115–125. doi: 10.1016/j.jmb.2004.02.034. [PubMed: 15050827]

Luther PK, 2000. Three-dimensional structure of a vertebrate muscle Z-band: implications for titin and alpha-actinin binding. J Struct Biol 129, 1–16. doi: 10.1006/jsbi.1999.4207. [PubMed: 10675292]

Mallick SP, Carragher B, Potter CS, Kriegman DJ, 2005. ACE: automated CTF estimation. Ultramicroscopy 104, 8–29. doi: 10.1016/j.ultramic.2005.02.004. [PubMed: 15935913]

Maupin-Szamier P, Pollard TD, 1978. Actin filament destruction by osmium tetroxide. J. Cell Biol 77, 837–852. [PubMed: 28332]

Milligan RA, Flicker PF, 1987. Structural relationships of actin, myosin, and tropomyosin revealed by cryo-electron microscopy. J. Cell Biol 105, 29–39. [PubMed: 3611188]

Morris EP, Nneji G, Squire JM, 1990. The three-dimensional structure of the nemaline rod Z-band. J Cell Biol 111, 2961–2978. [PubMed: 2269662]

Noble AJ, Stagg SM, 2015. Automated batch fiducial-less tilt-series alignment in Appion using Protomo. J Struct Biol 192, 270–278. doi: 10.1016/j.jsb.2015.10.003. [PubMed: 26455557]

Reedy MC, Reedy MK, Goody RS, 1987. The structure of insect flight muscle in the presence of AMPPNP. J Muscle Res Cell Motil 8, 473–503. [PubMed: 3443682]

Reedy MK, 1967. Cross-Bridges and Periods in Insect Flight Muscle. Am Zool 7, 465–481. doi: 10.1093/icb/7.3.465.

Reedy MK, 1968. Ultrastructure of insect flight muscle. I. Screw sense and structural grouping in the rigor cross-bridge lattice. J Mol Biol 31, 155–176. doi: 10.1016/0022-2836(68)90437-3. [PubMed: 5635532]

Reedy MK, Goody RS, Hofmann W, Rosenbaum G, 1983. Co-ordinated electron microscopy and X-ray studies of glycerinated insect flight muscle. I. X-ray diffraction monitoring during preparation for electron microscopy of muscle fibres fixed in rigor, in ATP and in AMPPNP. J Muscle Res Cell Motil 4, 25–53. [PubMed: 6841591]

Ribeiro Ede A Jr., Pinotsis N, Ghisleni A, Salmazo A, Konarev PV, Kostan J, Sjoblom B, Schreiner C, Polyansky AA, Gkougkoulia EA, Holt MR, Aachmann FL, Zagrovic B, Bordignon E, Pirker KF, Svergun DI, Gautel M, Djinovic-Carugo K, 2014. The structure and regulation of human muscle alpha-actinin. Cell 159, 1447–1460. doi: 10.1016/j.cell.2014.10.056. [PubMed: 25433700]

Rusu M, Hu Z, Taylor KA, Trinick J, 2017. Structure of isolated Z-disks from honeybee flight muscle. J Muscle Res Cell Motil 38, 241–250. doi: 10.1007/s10974-017-9477-5. [PubMed: 28733815]

Saide JD, Ullrick WC, 1973. Fine structure of the honeybee Z-disc. J Mol Biol 79, 329–337. doi: 10.1016/0022-2836(73)90009-0. [PubMed: 4760133]

Saide JD, Ullrick WC, 1974. Purification and properties of the isolated honeybee Z-disc. J Mol Biol 87, 671–683. [PubMed: 4214935]

Sainsbury GM, Hulmes D 1977. Notes on the structure of the Z-disk of insect flight muscle, pp. 75–76, *In* Tregear RT, (ed.) Insect Flight Muscle. Proceedings of the Oxford Symposium. North-Holland Publishing Company, Amsterdam.

Saxton WO, Baumeister W, 1982. The correlation averaging of a regularly arranged bacterial cell envelope protein. J Microsc 127, 127–138. doi: 10.1111/j.1365-2818.1982.tb00405.x. [PubMed: 7120365]

Schueder F, Mangeol P, Chan EH, Rees R, Schunemann J, Jungmann R, Gorlich D, Schnorrer F, 2023. Nanobodies combined with DNA-PAINT super-resolution reveal a staggered titin nanoarchitecture in flight muscles. Elife 12. doi: 10.7554/eLife.79344.

Squire JM, 1992. Muscle filament lattices and stretch-activation: the match-mismatch model reassessed. J Muscle Res Cell Motil 13, 183–189. doi: 10.1007/BF01874155. [PubMed: 1597512]

Squire JM, Bekyarova T, Farman G, Gore D, Rajkumar G, Knupp C, Lucaveche C, Reedy MC, Reedy MK, Irving TC, 2006. The myosin filament superlattice in the flight muscles of flies: A-band lattice optimisation for stretch-activation? J Mol Biol 361, 823–838. doi: 10.1016/j.jmb.2006.06.072. [PubMed: 16887144]

Suphamungmee W, Nakamura F, Hartwig JH, Lehman W, 2012. Electron microscopy and 3D reconstruction reveals filamin Ig domain binding to F-actin. J Mol Biol 424, 248–256. doi: 10.1016/j.jmb.2012.09.025. [PubMed: 23041423]

Taylor KA, Rahmani H, Edwards RJ, Reedy MK, 2019. Insights into Actin-Myosin Interactions within Muscle from 3D Electron Microscopy. Int J Mol Sci 20. doi: 10.3390/ijms20071703.

Thach RE, Thach SS, 1971. Damage to biological samples caused by the electron beam during electron microscopy. Biophys J 11, 204–210. doi: 10.1016/S0006-3495(71)86208-2. [PubMed: 5542613]

Toselli PA, Pepe FA, 1968. The fine structure of the ventral intersegmental abdominal muscles of the insect *Rhodnius prolixus* during the molting cycle. I. Muscle structure at molting. J. Cell Biol 37, 445–461. doi: 10.1083/jcb.37.2.445. [PubMed: 5656401]

Toyoshima C, 1989. On the use of holey grids in electron crystallography. Ultramicroscopy 30, 439–444. doi: 10.1016/0304-3991(89)90076-4.

Tregear RT, Edwards RJ, Irving TC, Poole KJ, Reedy MC, Schmitz H, Towns-Andrews E, Reedy MK, 1998. X-ray diffraction indicates that active cross-bridges bind to actin target zones in insect flight muscle. Biophys J 74, 1439–1451. doi: 10.1016/S0006-3495(98)77856-7. [PubMed: 9512040]

van Straaten M, Goulding D, Kolmerer B, Labeit S, Clayton J, Leonard K, Bullard B, 1999. Association of kettin with actin in the Z-disc of insect flight muscle. J Mol Biol 285, 1549–1562. doi: 10.1006/jmbi.1998.2386. [PubMed: 9917396]

Wang Z, Grange M, Wagner T, Kho AL, Gautel M, Raunser S, 2021. The molecular basis for sarcomere organization in vertebrate skeletal muscle. Cell 184, 2135–2150 e2113. doi: 10.1016/j.cell.2021.02.047. [PubMed: 33765442]

Wang Z, Hryc CF, Bammes B, Afonine PV, Jakana J, Chen DH, Liu X, Baker ML, Kao C, Ludtke SJ, Schmid MF, Adams PD, Chiu W, 2014. An atomic model of brome mosaic virus using direct electron detection and real-space optimization. Nat Commun 5, 4808. doi: 10.1038/ncomms5808. [PubMed: 25185801]

Winkler H, Taylor KA, 2006. Accurate marker-free alignment with simultaneous geometry determination and reconstruction of tilt series in electron tomography. Ultramicroscopy 106, 240–254. [PubMed: 16137829]

Wu S, Liu J, Reedy MC, Tregear RT, Winkler H, Franzini-Armstrong C, Sasaki H, Lucaveche C, Goldman YE, Reedy MK, Taylor KA, 2010. Electron tomography of cryofixed, isometrically contracting insect flight muscle reveals novel actin-myosin interactions. PLoS One 5, e12643. [PubMed: 20844746]

Xiong Q, Morphew MK, Schwartz CL, Hoenger AH, Mastronarde DN, 2009. CTF determination and correction for low dose tomographic tilt series. J Struct Biol 168, 378–387. doi: 10.1016/j.jsb.2009.08.016. [PubMed: 19732834]

Yamaguchi M, Izumimoto M, Robson RM, Stromer MH, 1985. Fine structure of wide and narrow vertebrate muscle Z-lines. A proposed model and computer simulation of Z-line architecture. J Mol Biol 184, 621–643. doi: 10.1016/0022-2836(85)90308-0. [PubMed: 4046026]

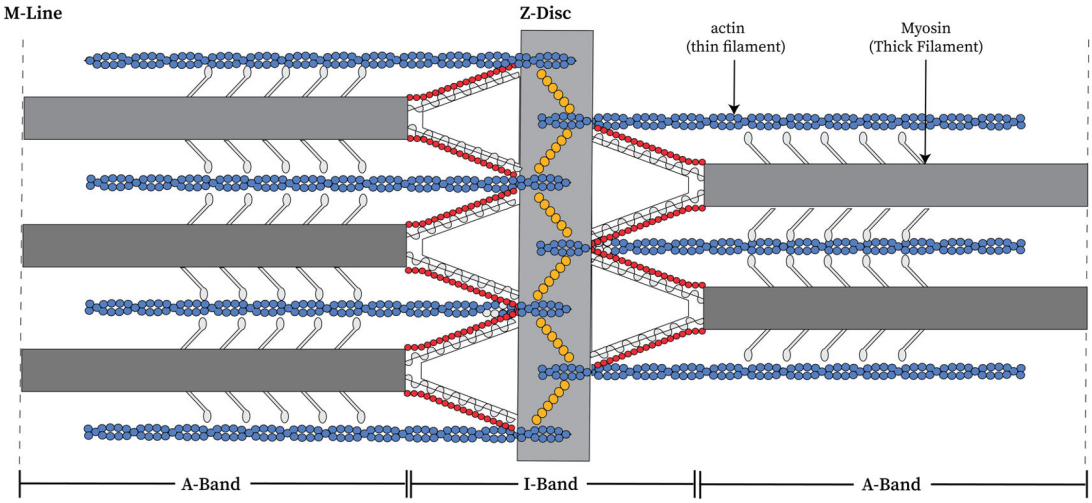

Figure 1. Diagram of the sarcomere structure.

The sarcomere is formed by the arrangement of actin and myosin filaments. The I-band of the sarcomere contains the area where actin filaments are not superimposed by myosin filaments. The A-band contains the overlap of actin and myosin filaments, and the H-zone within the A-band only contains the myosin filaments. The red structure connecting the ends of the thick filament to the Z-disk is kettin. The protein (uncolored) running with kettin is projectin. The gold structure crosslinking actin filaments of opposite polarity is α-actinin.

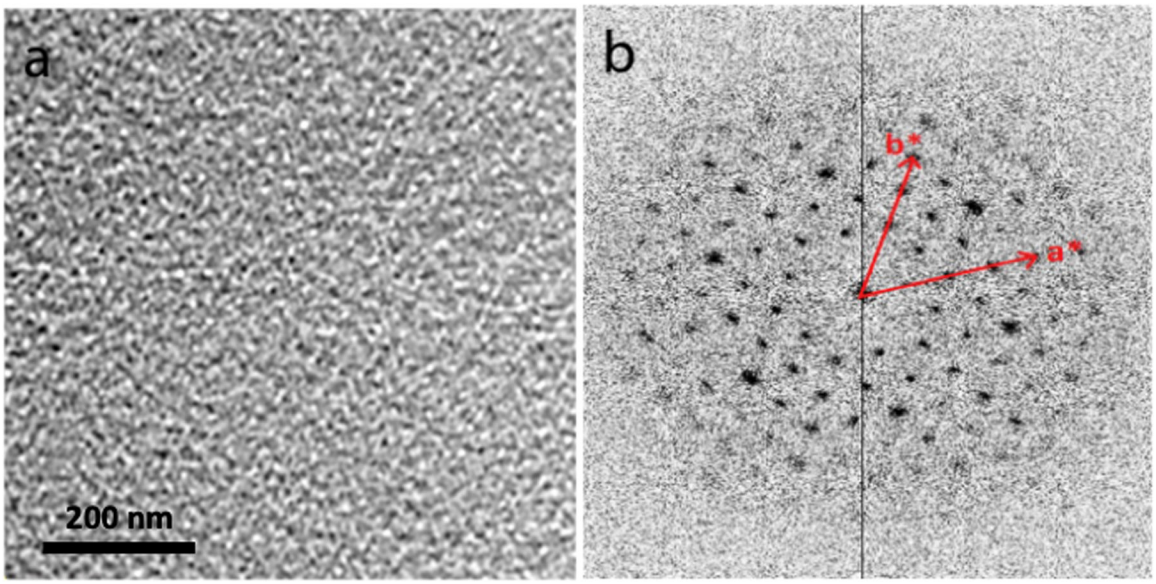

Figure 2. Raw tomogram of *Lethocerus* Z-Disc and Fourier transform at zero tilt angle.

(a) Section from the center of the raw tomogram. Raw tomograms were surprisingly noisy revealing little detail either in planes through the tomogram or projections of the tomogram. (b) Fourier transform of 0° tilt angle of (a). The *Lethocerus* Z-Disc produces a hexagonal diffraction pattern with spots spaced by 1/45 nm^{-1} or a spacing in real space of 52 nm. Typical transforms extend six orders or 7.5 nm resolution verifying that despite the noisy images, there is an ordered structure within the isolated Z-disk.

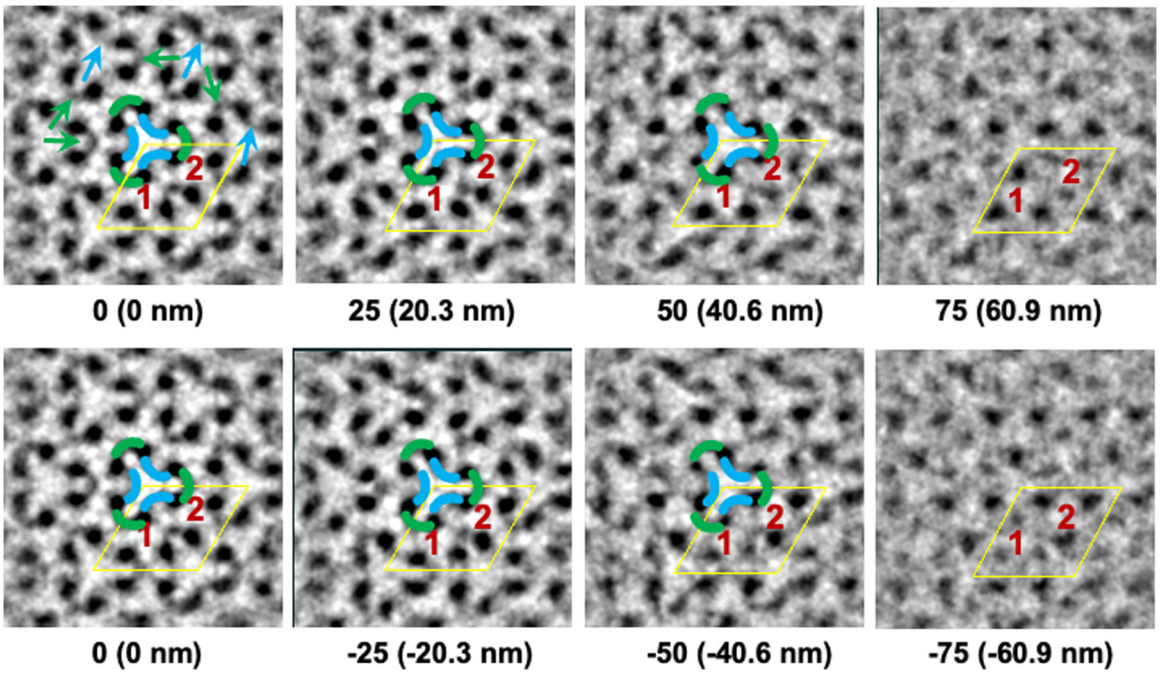

Figure 3. Sections from the global average tomogram from tilt series

A. Upper panel shows sections from 0 to +75 in steps of 25 and lower panel shows sections from 0 to −75. Each section has a pixel size of 0.812 nm, so the distance between the displayed sections is 20.3 nm. Protein is black; solvent is white. Black spots represent thin filaments. Some particularly easy to see connections between antiparallel thin filaments are indicated by green and cyan arrows, which correspond to connections between paired, antiparallel thin filaments indicated by green and cyan arcs. Connections between actin filaments generally appear light gray in the density map itself. They are of two types. One group, green, bows outward from the center of the channel. We identify this as the C1 connection of Cheng and Deatherage (1989). The other group, cyan, bows inwards. We identify this as the C2 connection of Cheng and Deatherage (1989). The unit cell is outlined in yellow. The numbers 1 & 2 represent antiparallel trimers of thin filaments at the trigonal positions.

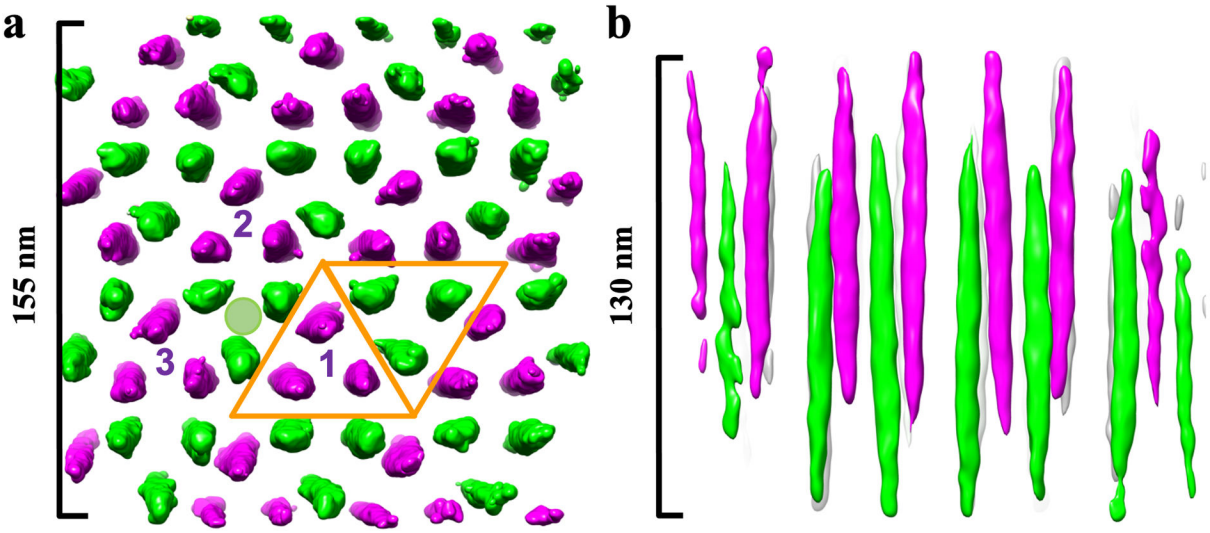

Figure 4. Arrangement of thin filaments in the *Lethocerus* Z-Disc.

(a) Top view of symmetrized global average of the *Lethocerus* Z-Disc showing the hexagonal arrangement of thin filaments. The unit cell is represented by the gold lines. Purple thin filaments represent those from sarcomere A while green thin filaments represent those from sarcomere B. A purple filament trimer located at the first trigonal position in the unit cell (labelled 1) is just to the right of a green filament trimer, the center of which is a thick filament position (green disk). The green thin filaments converge gently toward the thick filament positioned at the green disk. Two other purple trimers (labelled 2 and 3) surround the green thin filament trimer. Each of the three purple trimers contribute a pair of actin filaments that will surround this thick filament in the A-band. (b) Side view of Z-Disc showing the overlap and tilting of the filaments.

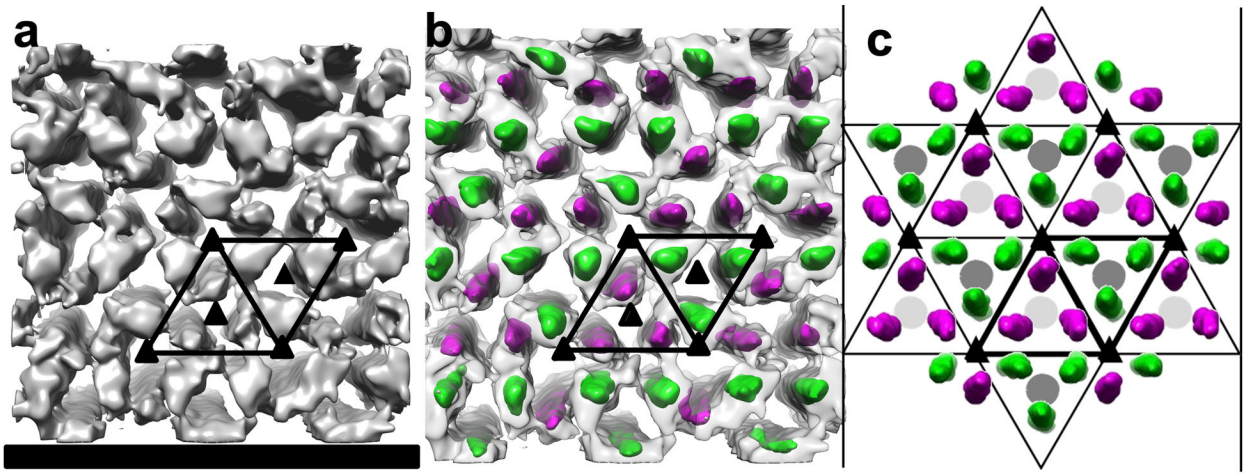

Figure 5. Density map of the global averages.

(a) Isosurface contour map (grey) of the symmetrized global average showing the connecting densities that form the Z-Disc. (b) Overlap of thin filaments from panel (c) (purple and green) on the transparent isosurface display. (c) Symmetrical arrangement of thin filament trimers about the unit cell edges. The dark and light grey disks represent the positions of the thick filaments in the A-band of adjacent sarcomeres. Green thin filament trimers converge toward the dark gray disks; purple thin filament trimers converge in the opposite direction toward the light gray disks. The unit cell in all the images are represented with thick black lines. Black scale bar = 155 nm. Note that in this view, all the solvent channels appear about the same diameter whereas the large and small solvent channels in *Apis* are of distinctly different sizes (Rusu et al., .2017).

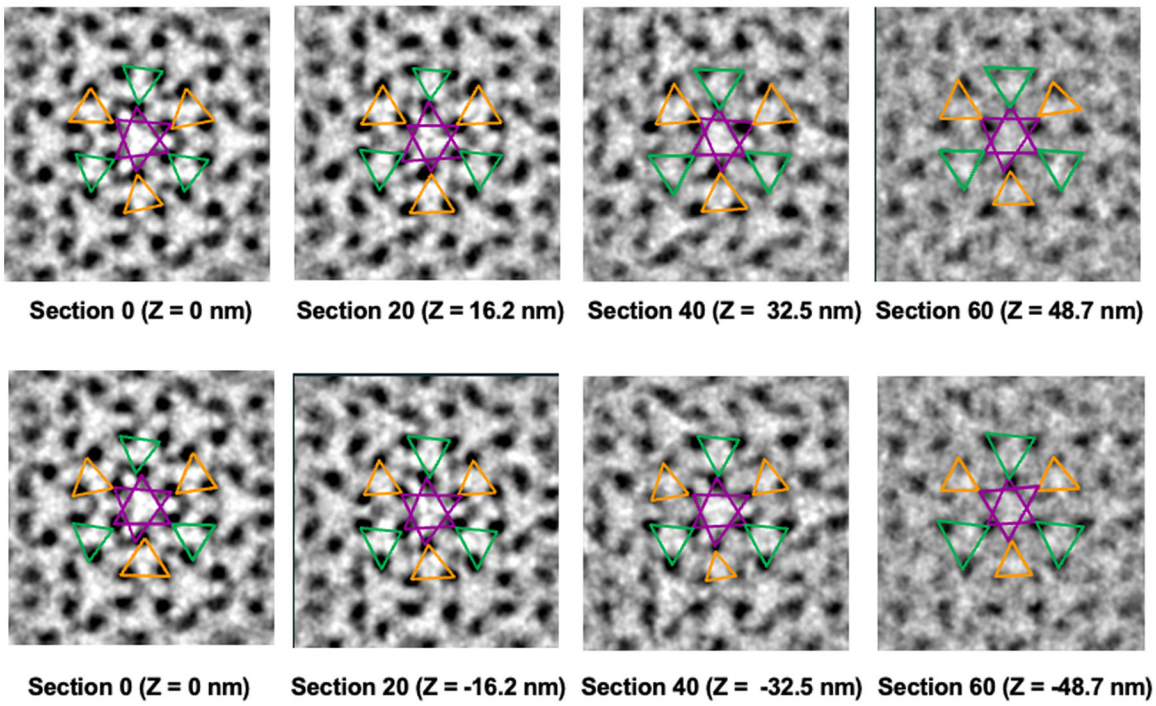

Figure 6. Comparison of the large and small solvent channels.

Upper panel shows sections from coordinates 0 to +60 and lower panel shows sections from 0 to −60. The physical distance between the displayed sections is 16.2 nm. The purple triangles represent the two groups of oppositely oriented actin filament trimers that comprise the large solvent channel. The gold and green triangles each represent the small solvent channels from either sarcomere A or B (1 or 2 as defined in Figure 4). The black spots are the thin filaments. The triangles representing the small solvent channel change little in size out to z = ±48.7 nm consistent with their small convergence angle towards the elastic connecting filament composed of Kettin and Projectin. The figure also illustrates that the thick filaments from one side of the Z-disk are not in-line with thick filaments from the other side but are offset by 30.0 nm along the diagonal of the unit cell.

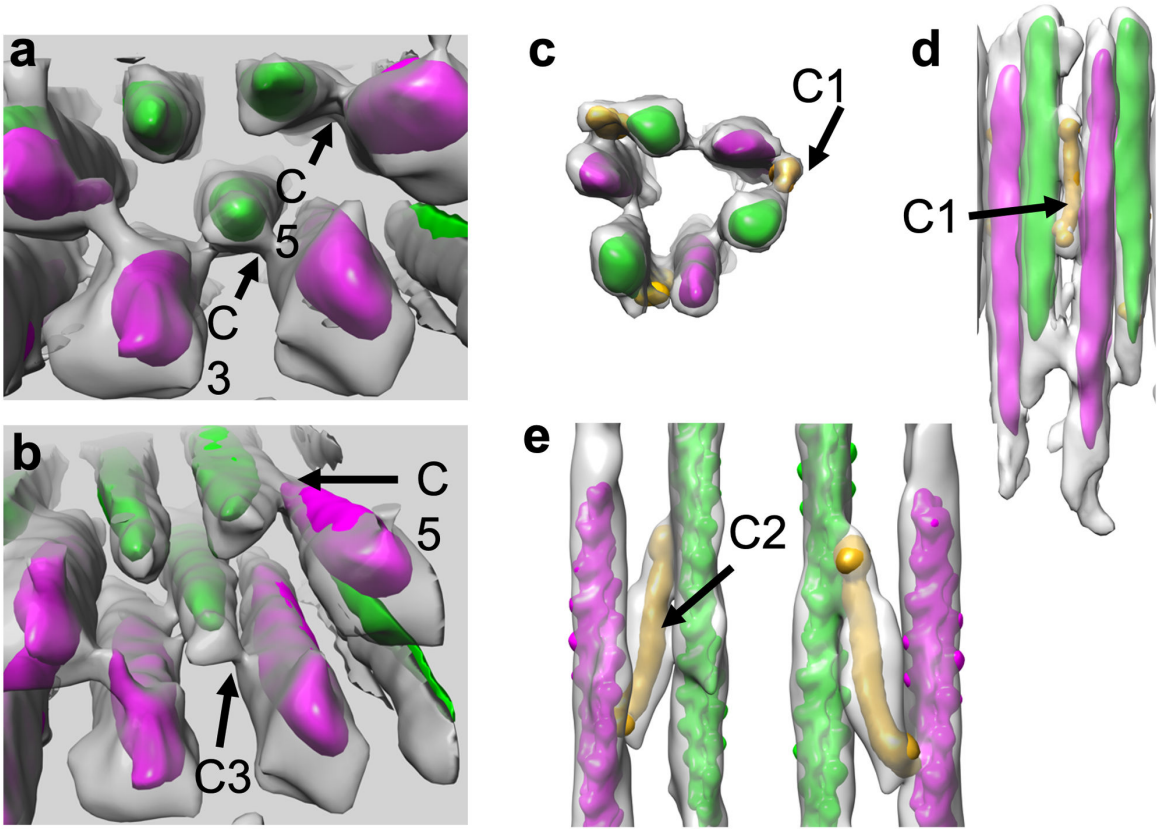

Figure 7. C1, C2, C3 and C5 connecting densities.

(a) Top view of C3 and C5. b) Oblique view of C3 and C5 at a lower contour threshold. Both densities (grey) connect the side of one thin filament (green) to another filament of opposite polarity (purple). (c) Top view of C1. Within the translucent envelope, a density map of α-actinin (yellow) can be fit reasonably well. Its axis is nearly parallel to the actin filaments it crosslinks. (d) Side view of panel *c*. (e) Front and back views of the C2 connection. Within the Z-disk density map envelope, a density map of α-actinin can be easily fit.

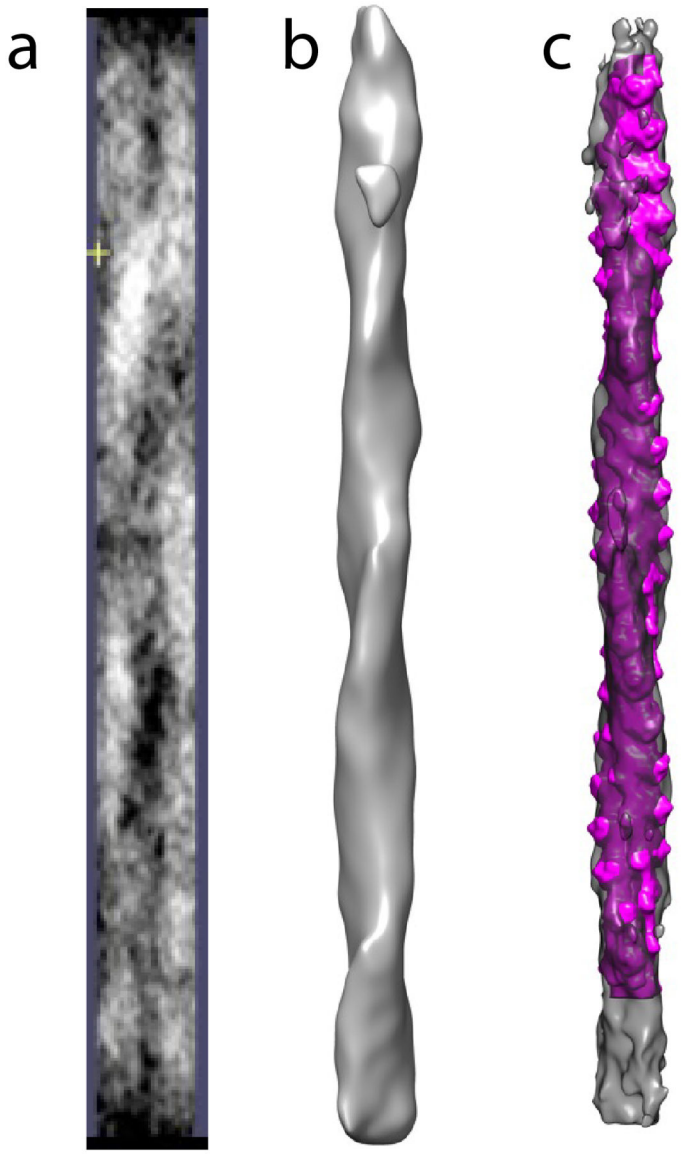

Figure 8. Masking of actin filaments in *Lethocerus* Z-Disc tomograms

a) Class average from multi-reference alignment that shows the long-pitch helix of the actin filament. b) Density map of a. c) Placement of F-actin density map (purple) into the experimental density map (b).

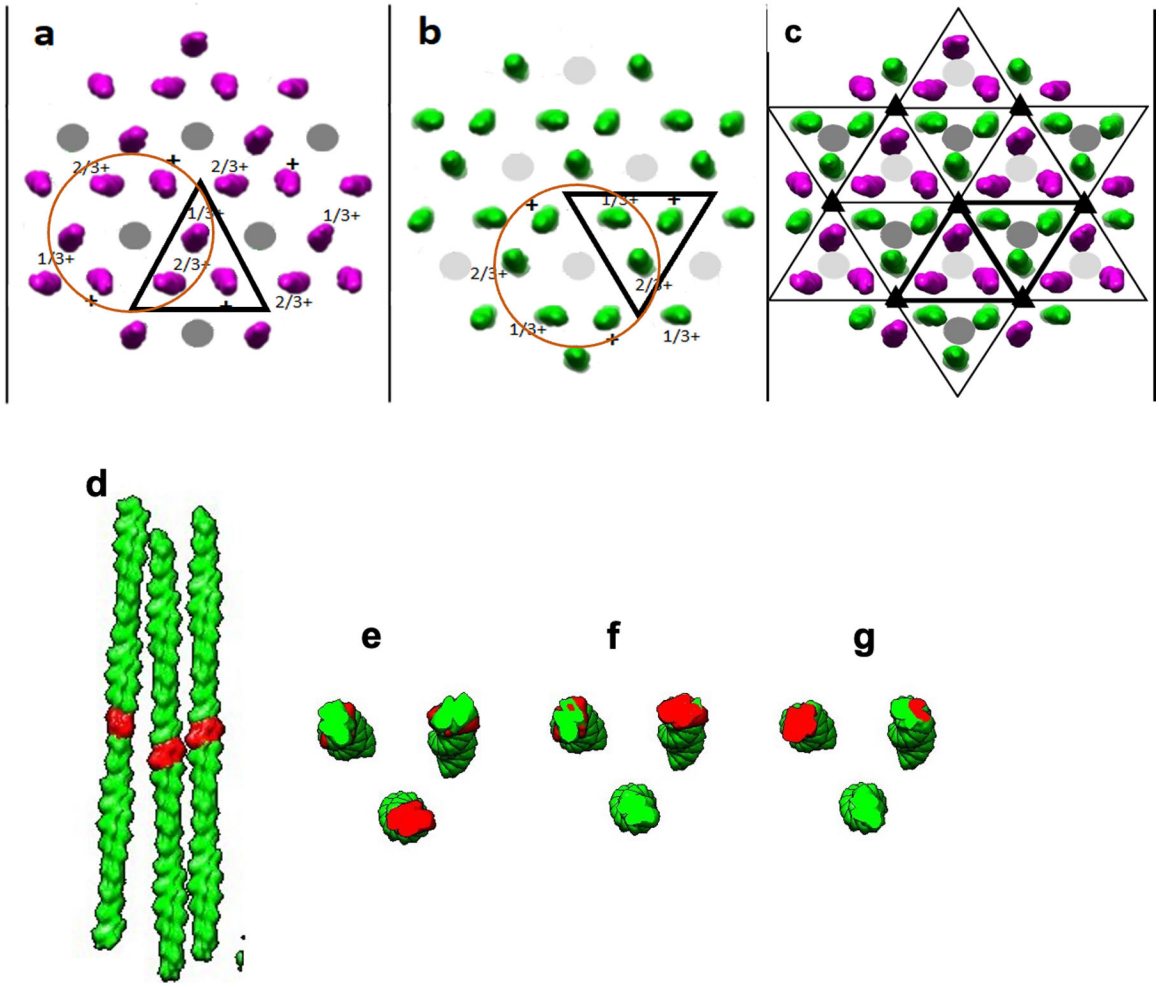

Figure 9. A-Bee-Z problem.

(a) Arrangement of thin (purple volumes) and thick filaments (grey disks) of an A-band in one sarcomere showing $P6_4$ symmetry within the brown circle (+, 1/3+, 2/3+, +, 1/3+, 2/3+). This is a left-handed screw symmetry. The left-handed screw symmetry about the thick filament results in a right-handed screw symmetry of the thin filaments within the trimers (+, 1/3+, 2/3+) (b) The arrangement of thin (green volumes) and thick filaments (gray disks) from the adjacent sarcomere also with $P6_4$ symmetry within the red circle. Oppositely oriented trimers of thin filaments when overlapped in the Z-disk show only approximate $P3_121$ symmetry (right-handed) within the triangle groupings of Z-disc shown in the black triangle because they are angled with respect to the axis as they pass through the Z-disk. c) overlap of *a* and *b* in Z-disc and unit cell. (d-g) Side view and top view of trimer at different z-depth. d) Side view of a trimer with most actin subunits colored green and one symmetry related actin subunit in red. (e-g) top view showing the location of the red subunit azimuthally. The subunit progresses axially from one filament to another in the trimer, but only by 2.75 nm, not the expected 12.9 nm.